

Modelling and measurement of piezoelectric fibres and interdigitated electrodes for the optimisation of piezofibre composites

L. J. Nelson^{*a}, C.R. Bowen^a, R. Stevens^a, M. Cain^b, M. Stewart^b

^aMaterials Research Centre, University of Bath, Bath, BA2 7AY, England.

^bMaterials Centre, National Physical Laboratory, Teddington, Middlesex, TW15 1UY, England.

ABSTRACT

Commercially available PZT-5A composition fibres fabricated using four production methods were incorporated into 1-3 composites with fibre volume fractions ranging from 0.02 to 0.72. Measurements of the piezoelectric induced strain constants (d_{33} and d_{31}), relative dielectric constants (ϵ_{33}), longitudinal coupling factors (k_{33}) and stiffness' (s_{33}) of the varying volume fraction composites are compared to analytical expressions in order to extract the fibre properties. Results show 1-3 composite data accurately follows the analytical trends. The Viscous Plastic Process (VPP) fibres are found to exhibit optimum material properties, which approach bulk material values. Reduced piezoelectric activity in extruded fibres is thought to be associated with a small grain size and high porosity. A second study, an optimisation of interdigitated electrode design, was performed using the finite element software ANSYS. The effect of the IDE geometry (electrode width and spacing) and PZT substrate thickness on the strain output of bulk PZT substrates was modelled. Results show optimal actuation occurs at electrode widths equal to half the substrate thickness, and for thin substrates the electrode finger spacing can be reduced to enable lower driving voltages.

Keywords: Piezoelectric, fibre, composites, interdigital, interdigitated, electrode, finite element analysis

1. INTRODUCTION

Fine scale piezoelectric lead zirconate titanate (PZT) fibres with diameters less than 250 μ m are not only finding uses in ultrasonic transducers¹ but in novel geometry composites, which comprise PZT fibres with interdigitated surface electrodes.² These composites, shown in Fig. 1, are commonly referred to as Active Fibre Composites (AFCs), Piezoflex or Macrofibre Composites (MFCs). They have potential uses as actuators and sensors,³ structural health monitoring systems⁴ and active/passive vibration damping systems.⁵ The ability to optimise the fibre properties and electrode geometry is necessary to optimise device performance, and will be the focus of this research.

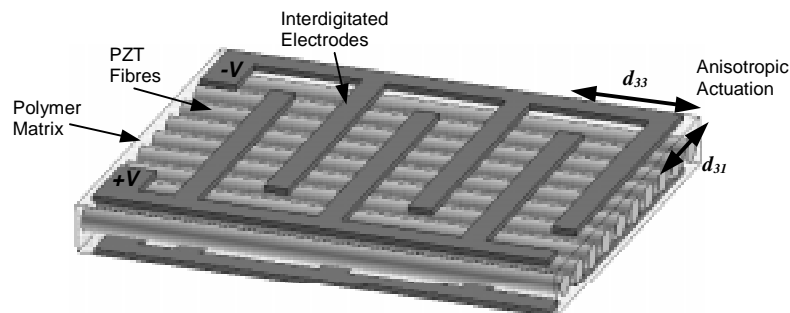


Figure 1: The construction of the active fibre composite, showing piezoelectric ceramic fibres, polymer matrix and interdigitated surface electrodes.

PZT fibres can be produced by numerous methods and a knowledge of the fibre properties are required for improving production processes and for selecting a production method for optimum fibre performance. However, small fibre diameters make common characterisation techniques difficult or impossible to use, thus little material property data is

* L.J.Nelson@bath.ac.uk; phone +44 1225385003; fax +44 1225386098

available. Commonly, fibre properties are determined by measuring the properties of 1-3 composites,^{6,7} which comprise aligned active fibres surrounded by a passive, typically polymer, matrix as shown in Fig. 2. By comparing the measured 1-3 composite properties with analytical equations it is possible to extract the fibre properties. This method is employed in the first part of this research (Section 2) which aims to characterise material properties of fibres manufactured by four different production methods.

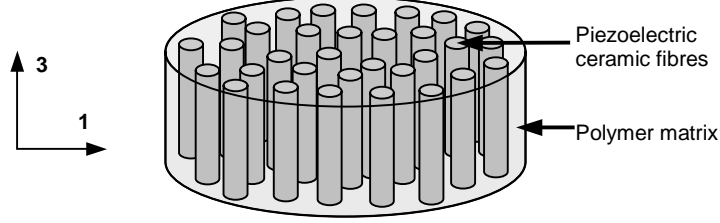


Figure 2: Schematic representation of a 1-3 piezocomposite comprising active piezoelectric ceramic fibres and a passive polymer matrix.

Analytical equations used to extract fibre data from 1-3 composite responses are given in Equations (1) to (6). In the derivation of these equations it is assumed that the composite spatial scale is sufficiently fine such that the composite can be treated as a homogeneous medium with effective material properties, which are a function of the material properties, and volume fractions of the constituent phases. Equations (1) to (6) show how the fibre properties (namely the piezoelectric induced strain coefficients d_{33} and d_{31} , the short circuit and open circuit compliances s_{33}^E and s_{33}^D , the constant stress permittivity ϵ_{33}^T and the longitudinal coupling factor k_{33}), and the polymer properties (namely the compliances s_{11} and s_{12} , and the permittivity ϵ_{11}), together with the fibre volume fraction v , determine the effective composite properties (denoted by a bar, e.g. \bar{d}_{33}).

$$\bar{d}_{33} = d_{33} \frac{vs_{11}}{vs_{11} + (1-v)s_{33}^E} \quad (1)$$

$$\bar{d}_{31} = v \left[d_{31} + d_{33} \frac{(1-v)(s_{12} - s_{13}^E)}{vs_{11} + (1-v)s_{33}^E} \right] \quad (2)$$

$$\bar{s}_{33}^E = \frac{s_{33}^E s_{11}}{vs_{11} + (1-v)s_{33}^E} \quad (3)$$

$$\bar{s}_{33}^D = \frac{s_{33}^D s_{11}}{vs_{11} + (1-v)s_{33}^D} \quad (4)$$

$$\bar{\epsilon}_{33}^T = v \left[\epsilon_{33}^T - d_{33}^2 \frac{(1-v)}{vs_{11} + (1-v)s_{33}^E} \right] + (1-v)\epsilon_{11} \quad (5)$$

$$\bar{k}_{33} = \left(1 - \frac{\bar{s}_{33}^D}{\bar{s}_{33}^E} \right)^{1/2} \quad (6)$$

For assumptions and detailed mathematical derivations of these equations the reader is guided to reference [8].

The ability to measure fibre properties, and therefore to select the best fibre production method, forms only part of the overall optimisation that can be achieved in the active fibre composite. A large factor determining actuation

performance is the geometry of the interdigitated electrode (IDE), which is used to direct the electric field to in-plane directions taking advantage of the d_{33} mode of actuation. Research on the effect of electrode geometry is limited^{9,10} and it is hoped that the finite element analysis presented in Section 3 will allow a greater understanding of factors that influence the strain output such as electrode finger width, electrode finger separation, and substrate thickness.

2. EVALUATION OF FIBRE PROPERTIES

2.1 Experimental

Lead zirconate titanate fibres (PZT-5A) as detailed in Table 1 were incorporated into 1-3 composites. The fibres were aligned in cylindrical moulds 2.0 mm in diameter and infiltrated with a low viscosity epoxy resin (Struers Specifix-40) under vacuum to reduce void formation. For high volume fraction composites ($\nu > 0.5$) the ceramic fibres were placed directly into the mould. Medium volume fractions ($0.2 < \nu < 0.5$) were manufactured by pre-coating the fibres with epoxy and allowing to cure prior to placing in the moulds. Mould filling with these coated fibres resulted in medium volume fraction composites comprising aligned and randomly distributed fibre arrangements. Low volume fraction composites ($\nu < 0.2$) were manufactured using a ‘pick and place’ technique. In this technique the fibres were partially inserted in a soft pliable modelling clay capable of holding the fibres vertically in the mould, which was subsequently filled with the resin. After curing overnight at 40°C the composites were cut to 5 mm lengths and polished on their end faces to ensure good electrical contact with the air dried silver paint which was subsequently applied. Poling was achieved by applying a field of 2.25 kVmm⁻¹ at 100°C for 10 minutes. The fibres were poled along their length and this is designated the 3-direction, while the 1-direction is orthogonal and in the samples radial plane (Fig. 2).

Table 1: Summary of the PZT-5A fibres tested.

Fibre Production Method	Diameter (microns)	Supplier
Extrusion ¹¹	130	CeraNova
Sol-Gel ^{12,13}	125 & 250	Smart Material Corp.
Viscous Plastic Processing (VPP) ¹⁴	250	IRC in Materials, Birmingham, UK
Viscous Suspension Spinning Process (VSSP) ¹⁵	235	Advanced Cerametrics

The polymer matrix permittivity ϵ_{11} and 1-3 composites constant stress permittivity ϵ_{33}^T were evaluated from capacitance measurements performed at 1kHz using a HP16451B dielectric test fixture attached to a HP4263B LCR meter. The matrix compliance s_{11} was obtained from the stress-strain plots of 2mm thick dumbbell specimens with a gauge length of 25mm. The tensile tests were performed on an Instron 1122 test machine at an extension rate of 0.5 mm/min. The matrix compliance s_{12} was calculated by estimating the Poissons ratio to be 0.38 ($s_{12} = -s_{11} \times \text{Poissons ratio}$)

Impedance analysis was used to determine \bar{k}_{33} , \bar{d}_{33} , \bar{s}_{33}^D and \bar{s}_{33}^E of the composites. The impedance of 1-3 composites was measured over the frequency range 150kHz to 500kHz with an excitation voltage of 500mV using an Agilent 4194A impedance analyser. This frequency range encompassed the fundamental resonance of the longitudinal-length mode associated with the sample geometry. Resonance and anti-resonance frequencies, f_r and f_a respectively, were recorded and used to calculate the effective material properties through equations appropriate for the longitudinal-length mode of resonance, Equations (7) to (10),¹⁶ in which l and ρ are the sample length and density.

$$d_{33} = k_{33} \left(\epsilon_{33}^T s_{33}^E \right)^{1/2} \quad (7)$$

$$k_{33} = \left[\frac{\pi}{2} \frac{f_r}{f_a} \cot \left(\frac{\pi}{2} \frac{f_r}{f_a} \right) \right]^{1/2} \quad (8)$$

$$s_{33}^E = \frac{s_{33}^D}{1 - k_{33}^2} \quad (9)$$

$$s_{33}^D = \frac{l}{4\rho f_s^2 l^2} \quad (10)$$

Measurements of \bar{d}_{31} were performed using a Take Control Piezometer. In this system the composites are loaded between two non-conducting ceramic studs, which make mechanical contact in the 1-direction and apply a 97Hz sinusoidal force of approximately 0.2N. The charge generated on the electroded ends of the composite is used to calculate \bar{d}_{31} .

Fibre microstructure (grain size and porosity) was characterised using a Jeol 6310 scanning electron microscope. Fractured ends were characterised because of the large differences in microstructure observed between fractured ends and fibre surfaces. This was especially noticeable in the extruded fibres where the surface microstructure suggests a larger grain size and reduced porosity compared to the fibre ends.

2.2 Results

Results of the effective properties of 1-3 composites versus fibre volume fraction are presented in Fig. 3, which show experimental results fit the analytical trends accurately. The results presented in Figure 3 are for 1-3 composites comprising 250 μ m diameter sol-gel fibres. The trend lines for \bar{d}_{33} and \bar{d}_{31} (Fig. 3(a) and 3(b) respectively) show that even at relatively low volume fractions the composites still retain a high percentage of the fibres piezoelectric activity. This is especially true for the coupling factor (Fig. 3(c)) where 80% of the fibre k_{33} value is retained in a composite containing only 5% fibres. Fig. 3(d) shows the dielectric constant varies essentially linearly with fibre volume fraction, except at low volume fractions. The slight suppression at low volume fractions is due to mechanical clamping of the ceramic fibres by the polymer matrix. Fig. 3(e) and 3(f) show that both the short circuit and open circuit compliances approach the fibre compliance with increasing fibre volume fraction.

Using the polymer material properties ($\epsilon_{11}/\epsilon_0 = 5$, $s_{11} = 357 \times 10^{-12} \text{Pa}^{-1}$ and $s_{12} = -136 \times 10^{-12} \text{Pa}^{-1}$) and the measured effective composite properties with Equations (1) to (6) the properties of the fibres were calculated. It was found that fibre properties calculated using low volume fraction composite measurements showed significant variations from fibre values calculated using the medium and high volume fraction composites, which were close to bulk PZT values. Errors in low volume fraction composites are likely to be inherently larger than high volume fraction composites. Resonance peaks tend to become broader as the fibre volume fraction is reduced, making accurate determination of the resonant and anti-resonant frequencies more difficult. Additionally, due to the smaller number of fibres being tested, the measured signals are weaker. Due to these errors, fibre properties were only determined from composites containing more than 20% fibres. The extracted fibre values, together with representative SEM images of the fibres microstructure, are presented in Fig. 4.

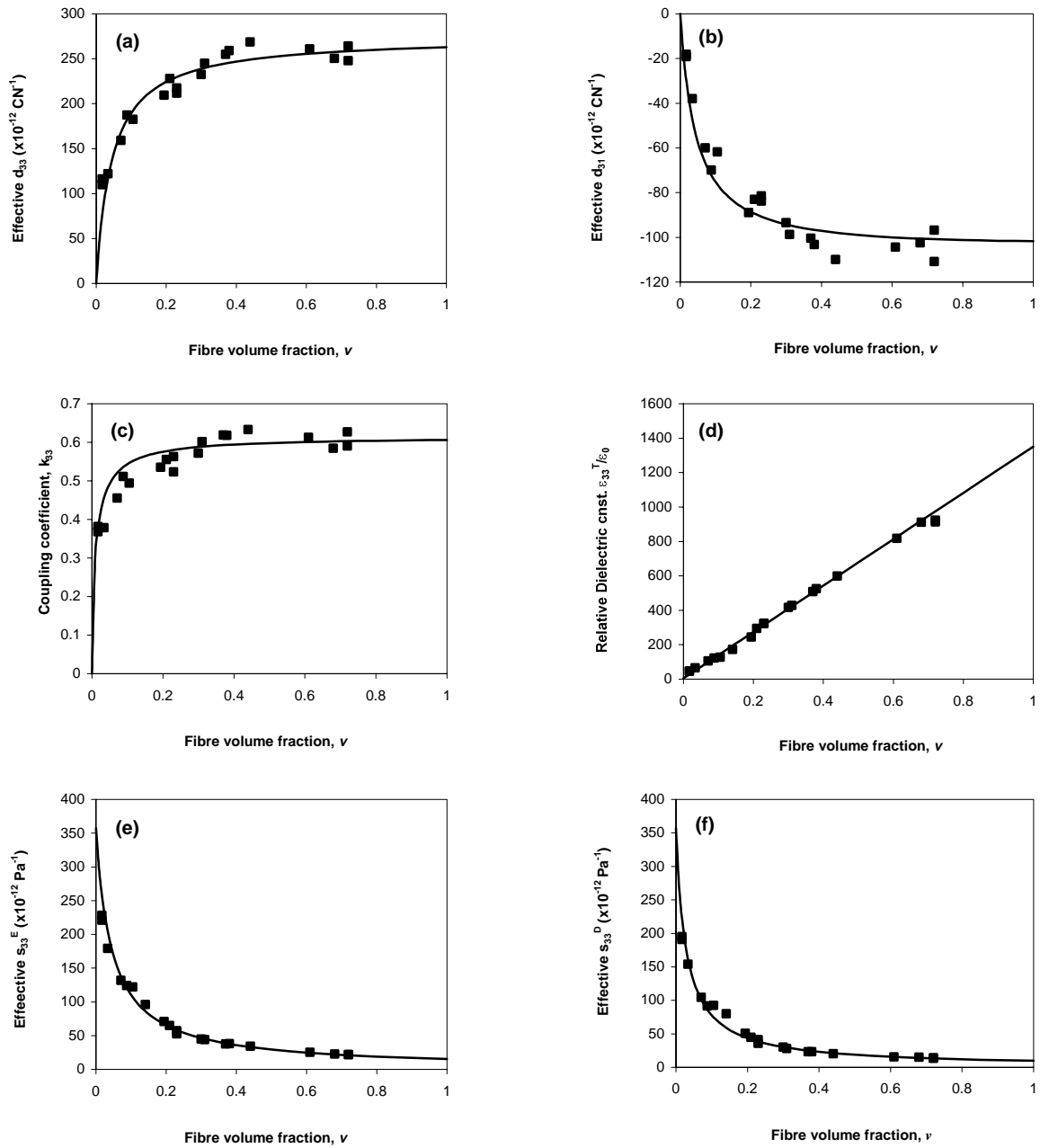


Figure 3: Experimental results of (a) effective d_{33} (b) effective d_{31} (c) effective coupling coefficient (d) effective relative dielectric constant (e) effective s_{33}^E and (f) effective s_{33}^D of 1-3 composites as a function of fibre volume fraction (ν). The effective property data is from composites manufactured with 250 μm diameter sol-gel fibres. The solid lines are the analytical models least squares fit to the data. The value of the trend line at $\nu=1$ represents the extracted fibre value.

The SEM images in Fig. 4 reveal that the fibre microstructure show considerable differences between fibre types. All but the sol-gel 125 μm fibres exhibit predominantly inter-granular fracture, with small amounts of trans-granular fracture apparent on the VSSP and VPP fibres. The sol-gel 125 μm fibres exhibit predominantly intra-granular fracture. The extruded and sol-gel 250 μm fibres show increased amounts of porosity and smaller grain sizes compared to the other fibres. It is interesting to note that the extruded and sol-gel fibres of small grain size show a reduced piezoelectric

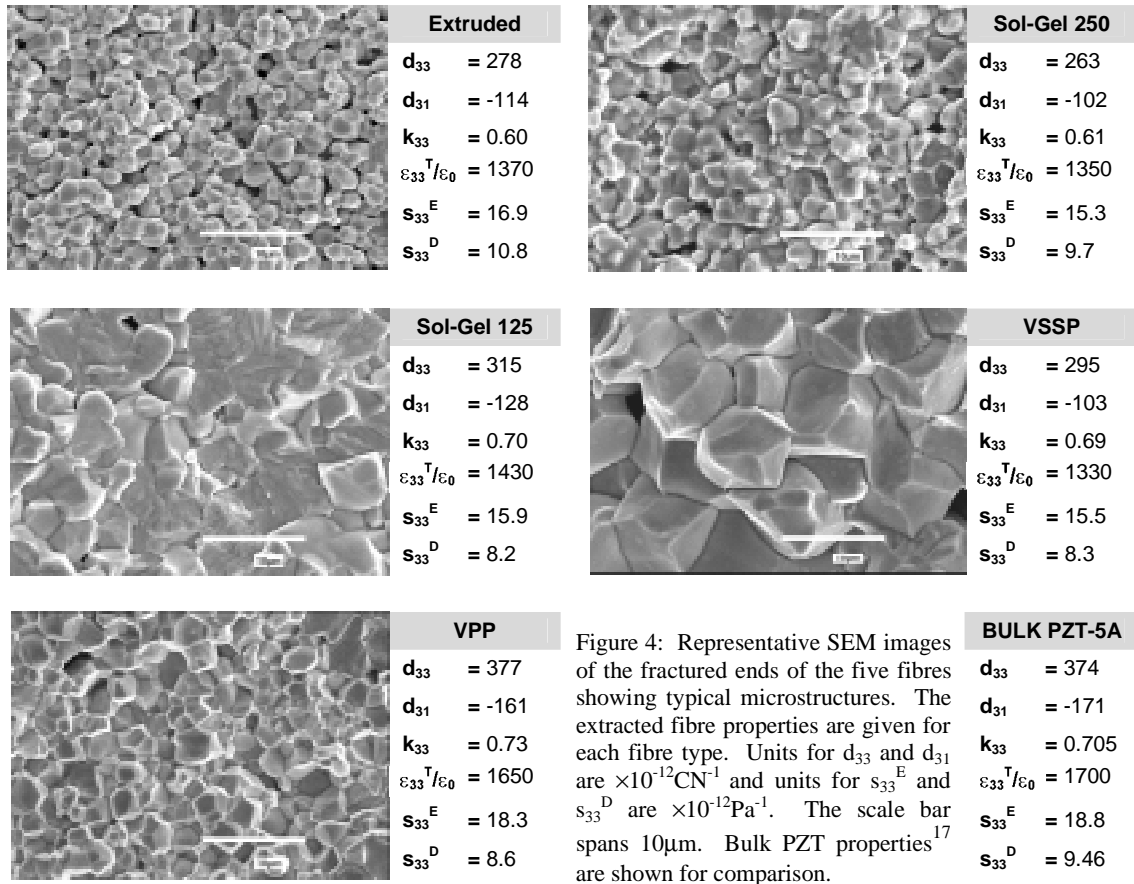


Figure 4: Representative SEM images of the fractured ends of the five fibres showing typical microstructures. The extracted fibre properties are given for each fibre type. Units for d_{33} and d_{31} are $\times 10^{-12} \text{CN}^{-1}$ and units for s_{33}^E and s_{33}^D are $\times 10^{-12} \text{Pa}^{-1}$. The scale bar spans $10\mu\text{m}$. Bulk PZT properties¹⁷ are shown for comparison.

activity, with d_{33} values of approximately 270pCN^{-1} and coupling factors of approximately 0.6, which are substantially lower than bulk values ($d_{33} = 374 \text{pCN}^{-1}$, $k_{33} = 0.71$). The sol-gel $125\mu\text{m}$ and VSSP fibre have a larger grain size, and reduced piezoelectric properties, compared to the VPP fibres. This suggests that an optimum grain size exists for which the piezoelectric and dielectric properties are maximised (VPP) and that excessively large (sol-gel $125\mu\text{m}$ and VSSP) or excessively small (extruded and sol gel $250\mu\text{m}$) grains cause a reduction in the piezoelectric properties. However, although all fibres are known to be PZT-5A the exact chemical composition, and hence ratio of tetragonal to rhombohedral phase, is unknown. It has been shown that the tetragonal to rhombohedral phase ratio strongly influences d_{33} , d_{31} , and ϵ_{33}^T of fibres,¹⁸ as in bulk PZT. Thus it is possible that the fibre composition may be responsible for the observed material property differences. Whatever the cause of the property variations it is clear that fibres produced by the VPP method exhibit the best piezoelectric properties. The short and open circuit compliances, s_{33}^E and s_{33}^D respectively, also show variation between the fibres with all fibres exhibiting stiffness greater than bulk PZT-5A. This has the benefit of increasing the fibres force capability as an actuator.

Two sources of error have been identified which may cause extracted fibre properties to differ from their true values. They are the frequency dependence of the polymer matrix mechanical properties, and the strength of the fibre matrix interface. Polymer mechanical properties are well known to be frequency dependent, becoming stiffer with increasing frequency. The matrix compliance in this study has been measured at low frequencies (an extension rate of 0.5mm/min) compared to the frequency at which the composite properties are being measured (150kHz to 500kHz for impedance analysis). At these higher frequencies the polymer is likely to be stiffer than the low frequency values suggest. Using low frequency compliance values as representative of the high frequency value will result in d_{33} , d_{31} , k_{33} , and the fibre compliance being underestimated. The degree to which these properties are underestimated is dependent on the volume fraction of the test sample. High volume fraction composite properties are less sensitive to the matrix mechanical properties and as such are less dependent on the test frequency. As the volume fraction is reduced the

composite properties become increasingly dominated by the matrix and as such will exhibit greater frequency dependence. However, since the matrix is already in its glassy state at room temperature an increase in frequency should only produce a relatively small increase in stiffness. The matrix clamping effect on the fibres, which are an order of magnitude stiffer, will therefore introduce negligible errors into the measured properties.

The uncertainty of the strength of the fibre-matrix interface forms the second source of error. In derivation of Equations (1) to (6) it is assumed that the matrix is perfectly bonded to the fibres. However, if the adhesion at the interface is poor the fibres will be less rigidly clamped. In this case the matrix can be considered as being more compliant, allowing the fibres to move more freely. Using the assumption of a perfect interface in a sample where the interface is weak will have the effect of overestimating d_{33} , d_{31} , k_{33} , and the fibre compliance. As yet the fibre-matrix interface strengths are unknown and as such errors introduced by this effect cannot be quantified.

3. OPTIMISATION OF INTERDIGITAL ELECTRODE DESIGN

3.1 Electrode Modelling

A schematic 2-D representation of an IDE on a bulk PZT substrate is shown in Figure 5(a), which illustrates the non-uniform electric field lines which are known to result from such an electrode geometry. Key parameters associated with the interdigitated electrode geometry are the electrode finger width (w) and electrode finger spacing (s). The electrode substrate thickness (t) has also been shown to influence device performance.^{9,10} The effect of these parameters on the actuation performance of a bulk PZT substrate was modelled using the finite element software ANSYS. The modelled representative volume element (RVE) is highlighted in Fig. 5(a). The expanded and meshed RVE is shown in Fig. 5(b) with appropriate dimensions. The surfaces are numbered for defining boundary conditions (Table 2).

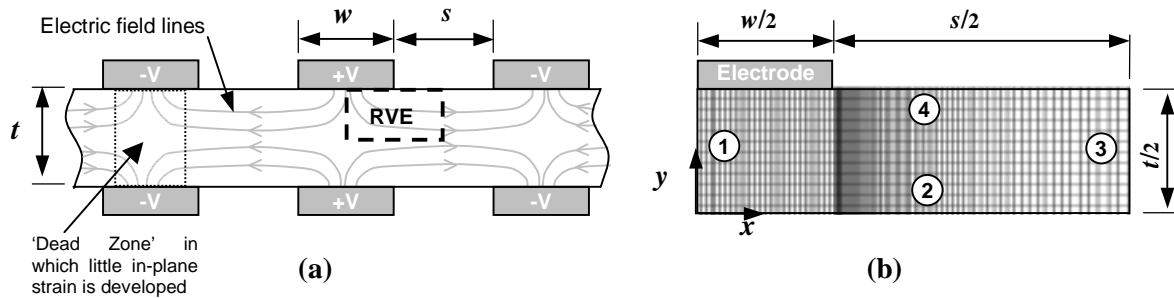


Figure 5: (a) 2-D interdigitated electrode schematic showing the electric field lines, geometry notation, and representative volume element (RVE). (b) RVE with numbered boundaries, appropriate dimensions and an example finite element mesh.

The model was constructed in the x - y plane, a necessity for 2-D modelling. The substrate was modelled as PZT-5A and meshed with 2-D coupled-field elements with piezoelectric capability. The element was set to plane strain conditions, implying that the model extends indefinitely in the z -direction. The element mesh size was set to be fine at the electrode edge to capture localised effects. The electrode in Fig. 5(b) was not modelled explicitly, but its presence was captured by the imposed electrical boundary conditions. Appropriate mechanical and electrical boundary conditions are detailed in Table 2.

Previous research^{9,10} has shown that the electric field direction within the substrate is non-uniform and will follow the field lines depicted in Fig. 5(a). Since poling of such IDE devices is performed using the IDEs, the direction of poling will follow these field lines, and the material properties will constantly change with respect to the model axis. It is not possible to model this variation in material property directionality in ANSYS thus the substrate was modelled as being uniformly poled in the x -direction. This simplification should prove adequate for large electrode separations in which the majority of the devices response will be attributed to the region between the electrodes, where the material is uniformly poled. However, differences between the modelled and actual responses at small electrode separations could exist as a result of this simplification.

Table 2: Boundary conditions of displacement (U) electrical potential (V) and electrical displacement (D) applied to the RVE.

Surface Number	Mechanical Conditions	Electrical Conditions
1	Symmetry ($U_x = 0$)	$D_x = 0$
2	Symmetry ($U_y = 0$)	$D_y = 0$
3	U_x coupled	$V = 0V$
4	Free	$V = +V/2$ on electrode, $D_y = 0$ elsewhere

Model dimensions were varied to investigate the effect of electrode finger width, electrode finger separation, and substrate thickness. The figure of merit used to assess the electrode geometry effects was chosen as the strain (S) developed in the x -direction per unit applied voltage. Plots of electric field strength in the x -direction at the substrate centre axis ($y = 0$) were also used to gain an insight into the influence of the IDE geometry.

3.2 Results

Results showing the effect of electrode width on the actuation performance are presented in Fig. 6. Fig. 6(a) shows that as the electrode separation is reduced the strain per unit applied voltage increases. This simply results from a higher electric field for a given voltage and does not necessarily advocate that small electrode separations increase performance, as will be highlighted when the electrode separation results are discussed. More importantly, this figure shows that there exists an optimum electrode width for which the strain per unit applied voltage is maximised, and that this width is independent of electrode separation and substrate thickness (data not shown in the figure). This optimum occurs at an electrode width equal to half the substrate thickness ($w/t = 0.5$), and deviation from this value has a greater effect on the strain at small separations. To understand why this optimum exists it is necessary to examine how the electric field in the substrate is affected by the electrode width at constant thickness and separation ($t = 200\mu\text{m}$, $s = 1\text{mm}$). Fig. 6(b) contains plots of electric field in the x -direction at the substrate centre axis ($y = 0$) for both the optimum w/t ratio, and for larger and smaller w/t ratios. For wide electrodes ($w = 400\mu\text{m}$, $w/t = 2$) the electric field strength in the x -direction between the electrodes is increased, but there also exists a high proportion of ‘dead area’ under the electrode, where the field in the x -direction is low. For thin electrodes ($w = 25\mu\text{m}$, $w/t = 0.125$) the proportion of dead area is lower, but the electric field in the x -direction is also low. The w/t ratio that induces optimum strain is a balance between the proportion of dead area under the electrode and the strength of electric field in the x -direction between the electrodes. As already stated, this optimum occurs at a w/t ratio of 0.5 ($w = 100\mu\text{m}$ in Fig 6(b)).

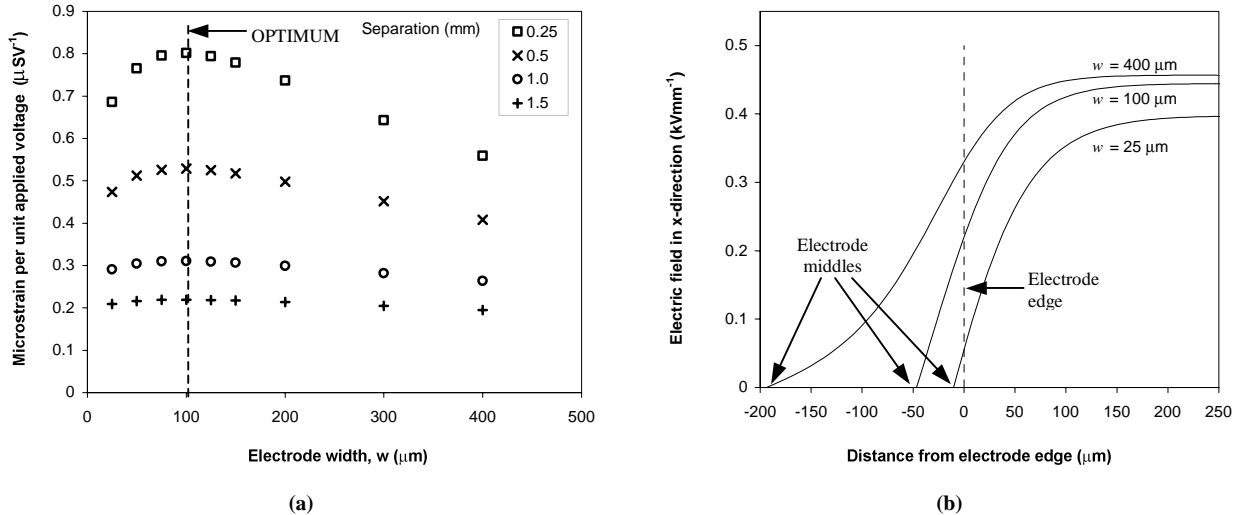


Figure 6: Finite element results for electrode width analysis showing (a) the effect of electrode width on the strain response of an interdigital electrode PZT substrate ($t = 200\mu\text{m}$) for four electrode separations, and (b) Path plots of electric field in x -direction at the substrate centre axis ($y = 0$) for three electrode widths ($t = 200\mu\text{m}$, $s = 1\text{mm}$, $V = 0.5\text{kV}$).

Results summarising the effect of substrate thickness are presented in Fig. 7. In this analysis the substrate thickness was varied while the electrode separation and w/t ratio were constant ($s = 1\text{mm}$, $w/t = 0.5$). Fig 7(a), which plots strain per unit applied voltage versus substrate thickness, highlights that reducing the substrate thickness increases the strain developed. The reason behind this is twofold, and can be seen by examination of Fig. 7(b), which shows electric field in the x -direction at the substrate centre axis for three substrate thicknesses. Firstly, as the substrate thickness is reduced the electric field becomes directed into the in-plane direction over a shorter distance, reducing the proportion of ‘dead area.’ Secondly, as the substrate thickness is reduced the electric field between the electrodes becomes larger. Both these effects result from opposing electrodes approaching closer as the substrate thickness is reduced, and thus exerting a stronger influence on one another. To quantify this effect, an approximate 17% increase in the strain per unit voltage can be expected when the substrate is reduced from a $200\mu\text{m}$ to $25\mu\text{m}$. This value does not account for other factors, such as the electrode separation, which is now discussed.

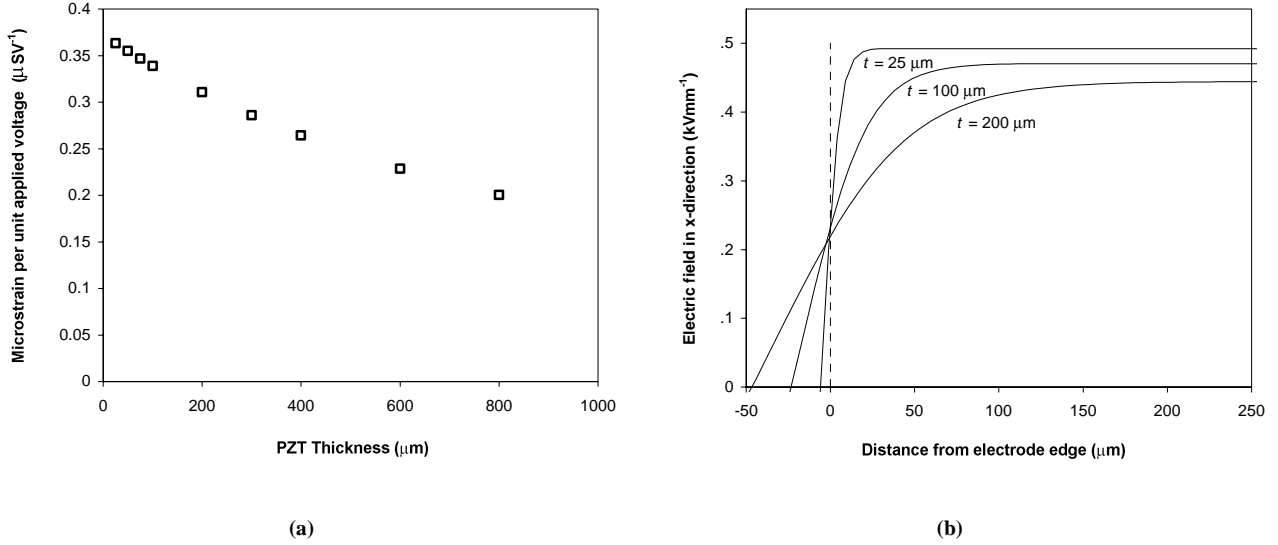


Figure 7: Finite element results for substrate thickness analysis showing (a) the effect of substrate thickness (for $w/t = 0.5$ and $s = 1\text{mm}$) on the strain response of an interdigital electrode substrate, and (b) Path plots of electric field in x -direction at the substrate centre axis ($y = 0$) for three substrate thicknesses ($w/t = 0.5$, $s = 1\text{mm}$, $V = 0.5\text{kV}$).

It has already been shown that dead zones exist below the electrode fingers, with the field being low and out of plane. With large electrode separations the proportion of dead zones is low, but the voltage required to operate the device is high. In contrast, small electrode separations reduce the operational voltage, but increase the proportion of dead zones. There exists a compromise between the actuation strain achievable and operational voltage. To investigate this effect a model with a fixed w/t ratio 0.5 was constructed, and the electrode separation was varied from 0.01 to 100mm. Fig. 8 summarises the results obtained. Fig. 8(a) shows the strain response as a function of electrode separation and contains two data sets, the first is from the finite element analysis and is and labelled ‘IDE response.’ This data shows that decreasing the electrode separation increases the strain, suggesting a small electrode separation is desired for increased actuation. However, this is misleading since this data fails to account for the reduction in actuation performance arising from the high percentage of dead area associated with small electrode separations.

To quantify the degradation in actuation performance the IDE strain response is compared to an idealised situation, in which the field is uniform and aligned in the actuation direction. For a block of piezoelectric material electrode on opposite faces separated by a distance s , the strain per unit voltage as a function of electrode separation will obey the relationship in Equation (11).

$$\frac{S}{V} = \frac{d_{33}}{s} \quad (11)$$

This strain response is also plotted in Fig. 8(a) and labelled as the ‘idealised response.’

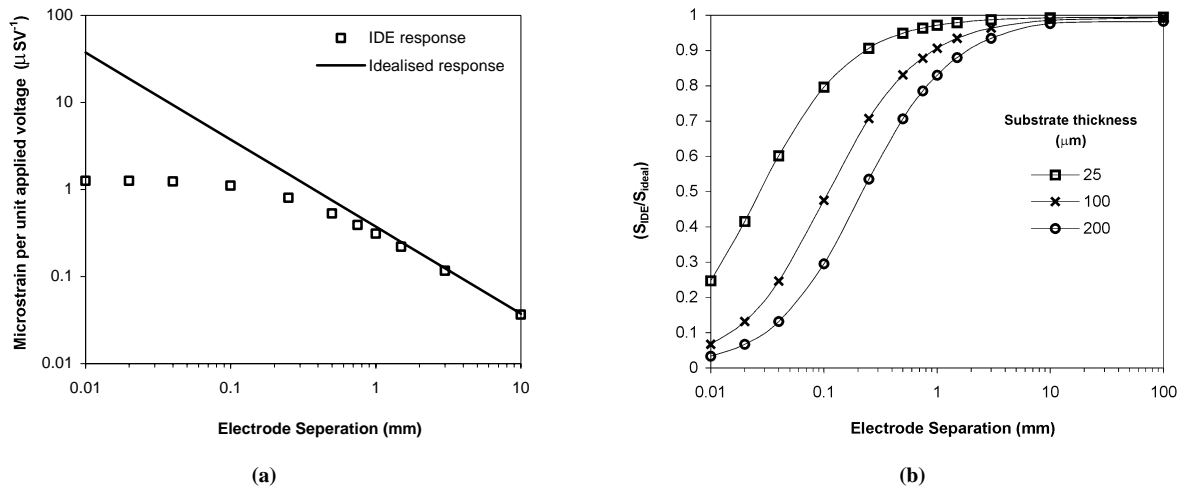


Figure 8: Results of the electrode separation analysis showing (a) the IDE and idealised strain response as a function of electrode separation, and (b) the strain response of an IDE substrate compared to that of the idealised strain response for three substrate thicknesses.

The deviation of the IDE strain S_{IDE} , from ideal response S_{ideal} , can be used to quantify the degradation in actuation resulting from the dead zones. This degradation is shown in Fig. 8(b), which plots S_{IDE}/S_{ideal} as a function of electrode separation for three PZT thicknesses. In all cases the electrode width was set so that $w/t = 0.5$. At large electrode separations the response is close to that of the ideal case. As the electrode separation is reduced the dead zones begin to dominate the response, and the IDE strain begins to diminish compared to the idealised response. Since a primary reason for using an IDE is to take advantage of the d_{33} response, which is approximately twice as large as the d_{31} response, once the reduction in actuation is greater than 50% this benefit is lost. From Fig. 8(b) it is apparent that for thinner PZT substrates the electrode separation can be reduced significantly while still maintaining a high percentage of d_{33} response. To obtain at least 80% of the d_{33} response electrode separations must satisfy $s/t > 4$. This condition requires electrode separations greater than 0.8 mm for a substrate thickness of 200 microns, reducing to separations of 0.1 mm for a substrate thickness of 25 microns. This is significant since a reduced electrode separation allows driving voltages, which are typically very high, to be reduced.

Modelling the substrate under the electrode finger region as un-poled, as has been the case in other research,⁹ would result in smaller strains than reported in this research. However, the electric field plots presented in Fig. 6(b) and Fig. 7(b) would be identical, thus trends in the strain response would be similar. The optimum electrode width would still occur at a w/t ratio of 0.5, reducing the substrate thickness will increase actuation, and for thin substrates the electrode spacing can be reduced while still maintaining a high percentage of the d_{33} actuation.

The extension of this work to fibre-matrix substrates used for active fibre composites (Fig. 1) implies small diameter fibres are desirable to enable production of thin substrates. Thus manufacturing techniques not only have to be capable of producing high quality fibres, but also fibres with small diameters.

4. CONCLUSIONS

Material properties of fibres produced by four manufacturing routes have been determined by measurements made on 1-3 composites. The trends in composite properties versus fibre volume fraction follow predicted trends accurately allowing fibre data to be extracted. Large variations in the properties between the fibres have been attributed to the observed differences in the microstructure, but compositional variations may also be a controlling factor. Extruded and 250μm sol-gel fibres, which have a small grain size and high porosity, exhibit severely reduced piezoelectric activity compared to bulk values. It is also possible that the reduced piezoelectric activity of the VSSP fibres is a result of an excessively large grain size. VPP fibres, which have grain sizes intermediate to the extruded and VSSP fibres, exhibit the highest piezoelectric activity, with values close to those for bulk PZT. This fibre production method, which has

been used to manufacture fibres with diameters down to 40 μm , has been identified as a preferred fibre production method, capable of producing semi-continuous fibres suitable for incorporation into active fibre composites.

Modelling of the interdigitated electrode structure on a bulk PZT substrate has given an insight into how the strain response is affected by electrode width, substrate thickness and electrode finger separation. The optimum strain was found to occur at an electrode width to substrate thickness (w/t) ratio of 0.5. A reduction in the substrate thickness has been shown to increase the strain output of the device by reducing ‘dead areas’ and increasing the field level between the electrode fingers. Finally, it was shown that 80% of the theoretical maximum strain can be achieved with an electrode separation to substrate thickness (s/t) ratio greater than 4. This has important implications since thin substrates allow smaller electrode separations, thus reducing the operational voltage. As a result of these findings it becomes clear that fibre manufacturing techniques not only have to be capable of producing high quality fibres, but also fibres with small diameters.

By understanding fibre properties and device architecture, efficient active fibre composites can be designed.

ACKNOWLEDGEMENTS

This work was funded by the University of Bath and the National Physical Laboratory. VPP fibres were kindly manufactured and supplied by Geoff Dolman, Bo Su and Tim Button, IRC in Materials Processing, School of Engineering, University of Birmingham, UK. Travel funds from the Armourers and Brasiers’ Company and British Alcan Aluminium are also gratefully acknowledged.

MATERIAL PROPERTY DATA

Table 3: Material property data for PZT-5A¹⁷ used for the finite element analysis in Section 3.

Material Property	Value
e_{33}	15.8 Cm^{-1}
e_{31}	-5.2 Cm^{-1}
e_{15}	12.3 Cm^{-1}
$\epsilon_{33}^T/\epsilon_0$	1700
$\epsilon_{11}^T/\epsilon_0$	1730
c_{11}^E	12.0×10^{10} Pa
c_{12}^E	7.52×10^{10} Pa
c_{13}^E	7.51×10^{10} Pa
c_{33}^E	11.1×10^{10} Pa
c_{44}^E	2.1×10^{10} Pa

REFERENCES

1. R. J. Meyer, Jr., T. R. ShROUT and S. Yoshikawa, “Development of ultra-fine scale piezoelectric fibers for the use in high frequency 1-3 transducers,” *Proc. 10th IEEE Int. Symp. On Applications of Ferroelectrics*, pp. 547-550, 1996.
2. L. J. Nelson, “Smart piezoelectric fibre composites,” *Materials Science and Technology*, **18**, pp. 1245-1256, 2002.
3. A. Schonecker, U. Keitel, W. Kreher, D. Sporn, W. Watzka and K. Pannkoke, “Smart structures by integrated piezoelectric thin fibres (II): Properties of composites and their physical description,” *Ferroelectrics*, **224**, pp. 7-12, 1999.
4. M. Schulz, M. Sundaresan and A. Ghoshal, “Active fiber composites for structural health monitoring,” In ‘Smart Structure and Materials 2000: Active materials: Behaviour and Mechanics,’ *Proc. of SPIE*, **3992**, pp. 13-24, 2000.
5. S. Yoshikawa, U. Selvaraj, K. G. Brooks and S. K. Kurtz, “Piezoelectric PZT tubes and fibres for passive vibration damping,” *Proc. 8th IEEE Int. Symp. on Applications of Ferroelectrics*, pp. 269-272, 1992.

-
6. R. Steinhausen, T. Hauke, W. Seifert, H. Beige, W. Watzka, S. Seifert, D. Sporn, S. Stark, A. Schonecker, "Fine scale piezoelectric 1-3 composites: Properties and modelling," *J. European Ceram. Soc.*, **19**, pp. 1289-1293, 1999.
 7. R. Steinhausen, T. Hauke, W. Seifert, H. Beige, U. Lange, D. Sporn, S. Gebhardt, A. Schonecker, "A new method for the determination of elastic properties of thin piezoelectric PZT fibres," *Ferroelectrics*, **268**, pp. 53-58, 2002.
 8. W. A. Smith, "Modelling 1-3 composite piezoelectrics: Hydrostatic response," *IEEE Trans. Ultrason., Ferroelec., Freq. Contr.*, **40** (1), pp. 40-47, 1993.
 9. D. J. Warkentin, "Modeling and electrode optimisation for torsional IDE piezoceramics," in 'Smart Structures and Materials 2000: Smart Structures and Intergrated Systems,' *Proc. of SPIE*, **3985**, pp. 840-54, 2000.
 10. N. W. Hagood, R. Kindel, K. Ghandi, P. Gaudenzi, "Improving transverse actuation of piezoceramics using interdigitated surface electrodes," in 'Smart Structures and Materials 1993: Smart Structures and Intelligent Systems', *Proc. of SPIE*, **1917**, 341-353, 1993.
 11. H. B. Strock, M. R. Pascucci, M. V. Parish, A. A. Bent, T. R. Shrout, "Active PZT fibres, a commercial production process," in 'Smart Structures and Materials 1999: Smart Materials Technologies,' *Proc. of SPIE*, **3675**, pp. 22-31, 1999.
 12. Q. F. Zhou, H. L. W. Chan, C. L. Choy, "Nanocrystalline powder and fibres of lead zirconate titanate prepared by the sol-gel process," *Journal of Materials Processing and Technology*, **63**, pp. 281-285, 1997.
 13. R. J. Meyer (Jr.), T. R. Shrout, S. Yoshikawa, "Lead zirconate titanate fibres derived from alkoxide-based sol-gel technology," *J. Am. Ceram. Soc.*, **81** (4), pp. 861-868, 1998.
 14. N. McN. Alford, J. D. Birchall, K. Kendall, "High-strength ceramics through colloidal control to remove defects," *Nature*, **330**, p. 51-53, 1987.
 15. R. B. Cass, J. D. French, "Developing innovative ceramic fibres," *J. Am. Ceram. Soc. Bull.*, **76** (5), 61-65, 1998.
 16. British Standard, "Piezoelectric properties of ceramic materials and components - Part 2: Methods of measurement - Low power," BS EN 50324-2, 2002.
 17. D. Berlincourt, H. H. A. Krueger, C. Near, "Properties of piezoelectric ceramics," Technical Publication TP-226, Morgan Electro Ceramics, Jan 2002.
 18. R. Steinhausen, T. Hauke, H. Beige, W. Watzka, U. Lange, D. Sporn, S. Gebhardt, A. Schnoecker, "Properties of fine scale piezoelectric PZT fibres with different Zr content," *J. European Ceram. Soc.* **21**, pp. 1459-1462, 2001.